

A Time-Resolved High-Resolution Spectroscopic Analysis of Ionized Calcium and Dynamical Processes in the Ultra-Hot Jupiter HAT-P-70 b

ADAM B. LANGEVELD,^{1,2} EMILY K. DEIBERT,³ MITCHELL E. YOUNG,⁴ ERNST DE MOOIJ,⁴ RAY JAYAWARDHANA,¹
CHRIS SIMPSON,⁵ JAKE D. TURNER,² AND LAURA FLAGG¹

¹*Department of Physics and Astronomy, Johns Hopkins University, Baltimore, MD 21218, USA*

²*Department of Astronomy and Carl Sagan Institute, Cornell University, Ithaca, NY 14850, USA*

³*International Gemini Observatory/NSF NOIRLab, Casilla 603, La Serena, Chile*

⁴*Astrophysics Research Centre, Queen's University Belfast, Belfast, BT7 1NN, UK*

⁵*Gemini Observatory, NSF's NOIRLab, 670 N A'ohōkū Place, Hilo, HI 96720, USA*

(Received 11 December 2024; Revised 12 February 2025; Accepted 15 February 2025 – ApJL)

ABSTRACT

We present the first transmission spectroscopy study of an exoplanet atmosphere with the high-resolution mode of the new Gemini High-resolution Optical SpecTrograph (GHOST) instrument at the Gemini South Observatory. We observed one transit of HAT-P-70 b – an ultra-hot Jupiter with an inflated radius – and made a new detection of the infrared Ca II triplet in its transmission spectrum. The depth of the strongest line implies that a substantial amount of Ca II extends to at least 47% above the bulk planetary radius. The triplet lines are blueshifted between ~ 3 to 5 km s^{-1} , indicative of strong dayside-to-nightside winds common on highly irradiated gas giants. Comparing the transmission spectrum with atmospheric models that incorporate non-local thermodynamic equilibrium effects suggests that the planetary mass is likely between 1 to $2 M_J$, much lighter than the upper limit previously derived from radial velocity measurements. Importantly, thanks to the high signal-to-noise ratio achieved by GHOST/Gemini South, we are able to measure the temporal variation of these signals. Absorption depths and velocity offsets of the individual Ca II lines remain mostly consistent across the transit, except for the egress phases, where weaker absorption and stronger blueshifts are observed, highlighting the atmospheric processes within the trailing limb alone. Our study demonstrates the ability of GHOST to make time-resolved detections of individual spectral lines, providing valuable insights into the 3D nature of exoplanet atmospheres by probing different planetary longitudes as the tidally locked planet rotates during the transit.

Keywords: Exoplanet atmospheres — High resolution spectroscopy — Transmission spectroscopy — Exoplanet atmospheric composition — Exoplanet atmospheric dynamics — Hot Jupiters

1. INTRODUCTION

The Gemini High-resolution Optical SpecTrograph (GHOST) is the new flagship high-resolution spectrograph at the Gemini South Observatory, Cerro Pachón, Chile (Ireland et al. 2012, 2014; McConnachie et al. 2024; Kalari et al. 2024). While designed to accomplish several key science objectives, it holds particu-

lar promise to deliver state-of-the-art optical spectra for in-depth characterization of transiting exoplanet atmospheres, both with transmission spectroscopy during the primary transit and emission spectroscopy at orbital phases around the secondary eclipse. GHOST's potential for such studies was demonstrated during the System Verification run in May 2023: with only ~ 3 hours of observations during the post-eclipse orbital phases of the ultra-hot Jupiter (UHJ) WASP-189 b, neutral iron was detected at a significance of 7.5σ , confirming the

presence of a thermal inversion in the planet’s dayside atmosphere (Deibert et al. 2024).

UHJs are typically tidally locked with short-period orbits in close proximity to hot (A- or F-type) host stars. Their permanent daysides receive intense stellar irradiation, causing temperatures to exceed ~ 2200 K and creating large day-to-night temperature gradients (Arcangeli et al. 2018; Bell & Cowan 2018; Parmentier et al. 2018). Observations and theoretical models have shown that these extreme conditions lead to exotic atmospheres composed of a diverse array of gaseous metallic atoms and ions (e.g. Kitzmann et al. 2018; Tabernero et al. 2021; Borsa et al. 2021; Borsato et al. 2023; Pelletier et al. 2023; Prinoth et al. 2024), together with strong winds and atmospheric flow from the dayside to the nightside (e.g. Showman et al. 2008, 2020; Rauscher & Kempton 2014; Heng & Showman 2015; Tan & Komacek 2019; Ehrenreich et al. 2020; Seidel et al. 2021). High-resolution spectroscopy has proven to be a powerful probe of UHJ atmospheres since it can resolve densely packed, narrow features that are imprinted within their transmission spectra due to absorption from chemical species. In particular, spectral features from the commonly detected refractory metal atoms and ions in UHJs are most prevalent at optical wavelengths.

“Time-resolved” high-resolution transmission spectroscopy (where a significant atmospheric signal is detected at multiple phases across the transit) is an innovative technique that offers unprecedented detail into 3D atmospheric composition and dynamics, but has typically only been feasible using cross-correlation focused methods (e.g. Ehrenreich et al. 2020; Kesseli & Snellen 2021; Gandhi et al. 2022; Pelletier et al. 2023; Prinoth et al. 2023; Wardenier et al. 2024; Simonnin et al. 2024). With this approach, hundreds of absorption lines from a particular chemical species are effectively averaged over the entire spectral range, significantly improving the signal-to-noise ratio (SNR). Such detections have led to the discovery of interesting phenomena with a temporal and spatial dependence, such as asymmetries in the atmospheric signals between the morning and evening terminators that could be explained by a multitude of physical mechanisms (e.g. Ehrenreich et al. 2020; Wardenier et al. 2021; Savel et al. 2022, 2023; Beltz et al. 2023; Nortmann et al. 2025). Performing the same time-resolved studies for individual absorption lines (without cross-correlating) is notably more difficult, because the spectra often need to be combined over the whole transit to make significant narrowband detections. However, pioneering efforts using the latest state-of-the-art spectrographs at 8–10 m telescopes have shown recent success (e.g. Seidel et al. 2023b; Prinoth et al. 2024).

GHOST’s high-resolution mode has a resolving power of $R \sim 76\,000$ and is able to obtain useful (throughput $> 2\%$) flux over a wavelength range of $\sim 3830\text{--}10\,000$ Å (Kalari et al. 2024), making it an ideal instrument for characterizing UHJ atmospheres. Further information about the design and specifications of GHOST, including overviews of both the “standard-resolution” and “high-resolution” modes, are presented by McConnachie et al. (2024) and Kalari et al. (2024).

During the GHOST Shared Risk run in December 2023, we observed one transit of the UHJ HAT-P-70 b to probe the terminator with high-resolution spectroscopy and investigate the chemical and dynamical processes across the boundary between the dayside and the nightside. HAT-P-70 b has an equilibrium temperature of ~ 2550 K, well above the ~ 2200 K transition between the “hot” and “ultra-hot” regimes. It resides on a near-polar orbit ($P = 2.74$ days) around a bright ($m_V = 9.5$) and rapidly rotating ($v \sin i = 99.85 \text{ km s}^{-1}$) A-type star, with a transit duration of 3.48 hours (Zhou et al. 2019) – a full list of system parameters can be found in Table A1. HAT-P-70 b is particularly conducive to transmission spectroscopy since it is one of the most inflated UHJs with a radius of $1.87 R_J$, and has a large transit depth ($> 1\%$), therefore acting as a great test case for this first transmission spectroscopy study with the high-resolution mode of GHOST.

One transit of HAT-P-70 b was previously observed with the High Accuracy Radial velocity Planet Searcher in the Northern hemisphere (HARPS-N) at the Telescopio Nazionale Galileo (TNG). Absorption features from several chemical species in the transmission spectrum were detected using the cross-correlation technique, and individual measurements were made for the strong optical absorption lines of hydrogen ($H\gamma$, $H\beta$, $H\alpha$), sodium (Na I doublet), and ionized calcium (Ca II H and K lines) (Bello-Arufe et al. 2022).

In this paper, we present new time-resolved detections of the infrared Ca II triplet lines, taking advantage of the wider wavelength coverage of GHOST and the increased SNR provided by the 8.1 m mirror of Gemini South. A full survey of chemical species in the transmission spectrum of HAT-P-70 b using these data will follow in the future. Information about the observations can be found in Section 2, and Section 3 outlines the transmission spectrum extraction. In Section 4 we present the detection of the Ca II triplet and discuss inferences that can be made about the upper atmosphere of HAT-P-70 b from both the combined and time-resolved transmission spectra, as well as comparison with atmospheric models. Our conclusion and outlook for future work can be found in Section 5.

2. OBSERVATIONS AND DATA REDUCTION

We observed one transit of HAT-P-70 b with GHOST/Gemini South on 2023 December 15 (Program GS-2023B-FT-105, PI: Langeveld) during the Shared Risk run. With the “high-resolution” mode, the target and the background sky were observed simultaneously.

GHOST has two arms (blue and red) – the full spectral range is divided at $\sim 5300 \text{ \AA}$ with a beam splitter, before the cross dispersion. Exposures from both the blue and red detectors were configured to start simultaneously to ensure that the same orbital phases were combined and analyzed together. Medium read modes were used for both detectors, with 1×4 (spectral \times spatial) binning to significantly decrease the readout times whilst maintaining the full spectral resolution. 140 pairs of exposures were acquired over ~ 5.5 hr, each with a 120 s exposure time – this consisted of ~ 3.5 hr for the transit and ~ 2 hr for the pre- and post-transit baseline. We aimed to achieve a SNR $\gtrsim 100$ over the majority of the spectral range whilst avoiding Doppler smearing of the planetary signal (Boldt-Christmas et al. 2024). Figure 1 shows the airmass variation and the average SNR for the blue and red arms throughout the sequence. One pair of exposures starting on 2023 December 16 at 04:10:03 (UT) was discarded due to a software restart after not acquiring slit images. Of the 139 remaining exposures, 87 were obtained during the in-transit phases, leaving 52 to build the high SNR out-of-transit baseline.

2.1. Data Reduction and Spectrograph Focusing

During the GHOST Shared Risk run, the spectrograph suffered from an issue where the focus was offset by $\sim 500 \mu\text{m}$ ($\sim 4\%$ different from the nominal value) for the red and blue science cameras. This resulted in an increase in inter-order flux, a loss of resolution, and artefacts appearing as periodic “ripples” visible in the extracted spectra. This was only a temporary issue experienced during the GHOST Shared Risk run; newer data acquired since then no longer exhibit the same problems as described here.

The data were reduced with version 1.1.1 of the GHOST Data Reduction (GHSTDR) software (Ireland et al. 2018; Hayes et al. 2022) utilizing the Data Reduction for Astronomy from Gemini Observatory North and South (DRAGONS) platform (Labrie et al. 2023). GHSTDR v1.1.1 has an improved reduction algorithm designed specifically to account for the unfocused Shared Risk data. Namely, it Gaussian smooths the slit profile from the slit-viewer camera (which was in focus) to more accurately represent the profile seen by the spectrograph, and uses different regions of the slit to extract the object and sky spectra. This decreased

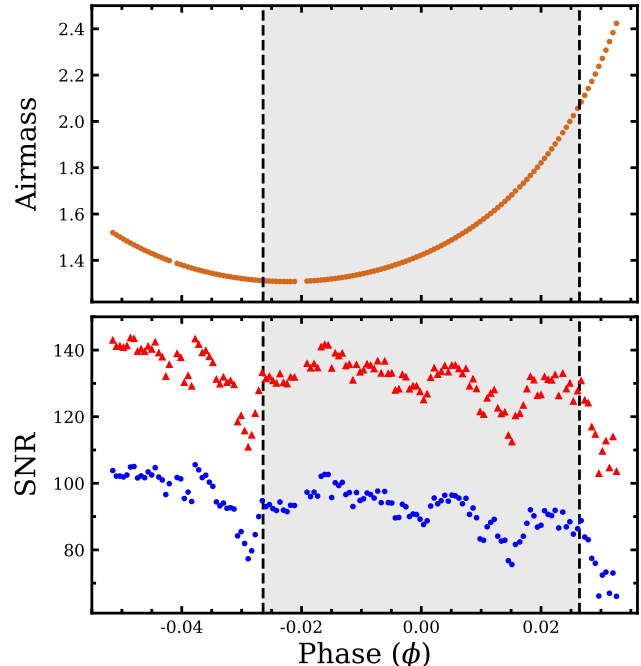


Figure 1. *Top panel:* Change in airmass throughout the observations. One exposure was discarded during the transit. There was a temporary loss of guiding during the pre-transit sequence. *Bottom panel:* Average SNR across the full spectrum for each blue and red exposure (marked with blue circles and red triangles respectively). The black dashed lines and grey shaded region highlight the in-transit phases.

the magnitude of the spurious artefacts in the extracted spectra (compared to GHSTDR v1.1.0), retaining them only at a 1–2% level. The location of these artefacts did not change significantly throughout the night, causing minimal impact on our analysis of the extracted exoplanetary spectra (see Section 3).

The DRAGONS/GHSTDR pipeline takes the blue and red detector images and performs the bias subtraction, bad pixel masking, and flat-fielding. Then, the observed spectrum is optimally extracted with cosmic-ray rejection (including optional sky subtraction), and a wavelength solution and optional barycentric correction are applied, to produce outputs in both 2D (a spectrum for each order) and 1D (a single spectrum with all orders merged) form, resulting in two data products for each arm. We opted to reduce the data with the sky subtraction and barycentric correction turned off since (a) no significant features were visible in the sky spectrum in the region of the Ca II triplet, and (b) we require the spectra to be in the Earth rest frame for accurate telluric correction (see Section 3).

The impact of the unfocused spectrograph is still being assessed; we hypothesize that it could result in the planetary atmospheric signals being slightly broadened, or imperfect corrections to the ripples causing the line

shapes to be distorted. Therefore, in this study, we choose to demonstrate GHOST’s capability for time-resolved transmission spectroscopy of individual absorption lines for only one chemical species (the Ca II triplet). Following a robust assessment of the focusing implications, a full survey of the atmospheric chemistry of HAT-P-70 b will follow in future work.

3. TRANSMISSION SPECTROSCOPY

We took the 1D data products from the DRAGONS/GHOSTDR pipeline and followed the methods described in [Langeveld et al. \(2022\)](#) to clean and process the data and extract the transmission spectrum of HAT-P-70 b. Minor changes to the pipeline are outlined below. The blue and red arms of GHOST were treated independently using the same methods, except when generating the telluric models (see below).

Telluric contamination was removed by generating models of the transmission through Earth’s atmosphere with `molecfit` version 4.3.1 ([Smette et al. 2015](#); [Kausch et al. 2015](#)), which has been applied successfully for many previous studies of exoplanet atmospheres with high-resolution spectroscopy (e.g. [Allart et al. 2017](#); [Langeveld et al. 2021](#)). Since the blue arm of GHOST covers wavelengths relatively devoid of strong telluric lines, the blue and red spectra were joined together to produce one telluric model per exposed phase; the data were cut at 5350 Å and the blue spectra were scaled to the same level as the red by matching the medians of the last 500 blue flux values to the first 500 red flux values. This is justified given that both detectors were configured to start and end each exposure simultaneously, thus covering the same time interval and airmass range. The resulting `molecfit` model was interpolated back onto the original wavelength grid of the separate blue/red spectra and divided out to remove the telluric contamination. The region encapsulating the Ca II triplet only contains weak tellurics ($\gtrsim 0.95$ transmission); thus, for this study, there are no issues with the model failing to provide an accurate correction for very deep lines.

We accounted for Doppler shifts due to Earth’s barycentric radial velocity and the systemic velocity, but not the stellar radial velocity due to the uncertainty in the mass of HAT-P-70 b and the fact that it is a rapidly rotating star with broad spectral lines. The stellar components of the spectra were then removed by dividing by a master out-of-transit spectrum (the weighted average of all out-of-transit spectra, with each flux value assigned a weight of $1/\sigma^2$), resulting in “residual spectra” – the in-transit residuals contain the exoplanet’s atmospheric transmission features (plus noise) and the out-of-transit residuals represent only the noise.

Individual absorption lines from various chemical species are typically too weak to be visible over the noise in the residual spectra, but they should follow a sinusoidal path due to the orbital motion of the planet – during the transit, this path is a diagonal line between the phases of the first and fourth transit contact points. However, thanks to the high SNR achieved by GHOST/Gemini South, strong features such as the Ca II triplet lines are remarkably visible across the whole time series, as shown in [Figure 2](#). Such clear “time-resolved” detections of single lines have only become achievable on a wide scale in recent years with 8–10 m class telescopes and state-of-the-art high-resolution spectrographs (e.g. ESPRESSO/VLT and MAROON-X/Gemini North: [Seidel et al. 2023b](#); [Prinoth et al. 2024](#)). Therefore, this demonstration places GHOST among the few instruments that can achieve the required SNR to conduct such studies and analyze how the absorption features vary in time.

The top row of [Figure 2](#) also shows spurious signals imprinted within the transmission spectra due to the Rossiter-McLaughlin (RM) effect, which follow a diagonal path in the opposite direction to the planetary trail (for further discussion, see, e.g. [Rossiter 1924](#); [McLaughlin 1924](#); [Gaudi & Winn 2007](#); [Triaud 2018](#); [Prinoth et al. 2024](#)). These signals can result in false detections of atmospheric species (e.g. [Casasayas-Barris et al. 2020, 2021](#)), so must be removed to fully assess the extent of absorption in the planetary atmosphere. As seen in [Figure 2](#) (top row), the RM signals have a similar amplitude as those from the planetary atmosphere, evident by the overlapping region near the transit ingress where the RM and atmospheric features essentially cancel each other out. We modelled the RM effect and centre-to-limb variations (CLV) using the same grid-based approach as in [Turner et al. \(2020\)](#) and [Deibert et al. \(2021\)](#). However, given the large extent of the planet in the Ca II lines, which is not accounted for in this model, there is a strong residual signal during the phase range where the planet’s signal overlaps with the RM signal. Correcting for this would require a model that simultaneously accounts for the planet’s atmosphere and the wavelength-dependent RM effect (e.g. [Dethier & Bourrier 2023](#)), which is beyond the scope of this work. We therefore masked out this region, following some other studies that have measured time-resolved signals (e.g. [Borsa et al. 2021](#); [Kesseli et al. 2022](#); [Simonnin et al. 2024](#)), as shown in the second row of [Figure 2](#).

Finally, each spectrum was Doppler shifted into the planetary rest frame using radial velocity values calculated from the parameters listed in [Table A1](#), and subtracted by 1 (e.g. [Wytttenbach et al. 2015](#); [Langeveld](#)

et al. 2022). Then, all fully in-transit phases (where at least some of the planet is transiting for the entire exposure duration) were combined with a weighted average (weights = $1/\sigma^2$ for all flux values). The result is a single high SNR transmission spectrum that represents the average atmospheric absorption over the whole transit, shown in Figure 2 (bottom panel).

We note that there are some residual patterns visible in the top panels of Figure 2, between phases of -0.05 and -0.04, which likely originate from imperfect corrections of the ripples in the out-of-focus data. We performed the same analysis as described above while ignoring these few spectra, and found that there was no significant change in the extracted transmission spectrum and the results discussed in Section 4.

4. RESULTS AND DISCUSSION

4.1. *The Combined Transmission Spectrum of HAT-P-70 b: Ca II Triplet Lines*

The bottom row of Figure 2 shows the combined transmission spectrum around the infrared Ca II triplet, representing the average absorption over the full transit. All three Ca II lines are clearly resolved and detected at high SNR. In the rest frame of the planet, the three lines should be located at 8498.02, 8542.09, and 8662.14 Å (marked with the blue dashed lines). We took the standard approach to fit Gaussian profiles to each absorption line, and from this, measured their absorption depths (δ), observed (line of sight) velocity offsets of the line centroids from their rest-frame locations, and full width at half maximum (FWHM) – the results are shown in Table 1.

Using Equation (13) from Langeveld et al. (2022), the measured absorption depths (δ) from Table 1 can be converted to relative atmospheric heights (normalized to R_p) at which most of the absorption occurs. For the deepest line at 8542.09 Å, with a depth of $(-1.22 \pm 0.03)\%$, the corresponding relative atmospheric height is 0.47 ± 0.02 – i.e. the radius of the planet at this wavelength appears to be 47% larger than the white-light planetary radius due to the absorption occurring within the atmosphere.

The uncertainty in the mass of HAT-P-70 b, where only an upper limit ($M_p < 6.78 M_J$) has previously been measured, makes it difficult to quantify if the atmospheric layer probed by Ca II is escaping. However, using the upper limit for the planetary mass, the Roche lobe radius approximately extends to $\sim 3.9 R_p$ (Eggleton 1983). The strongest Ca II absorption line would only indicate atmospheric escape if the mass of the planet is less than $0.4 M_J$. Therefore, it is unlikely that this

Table 1. The depths, velocity offsets (deviation from the rest frame wavelengths), and FWHM of the detected Ca II triplet lines, measured from Gaussian fits to each line.

Ca II line λ (Å)	Depth δ (%)	Velocity (km s ⁻¹)	FWHM (km s ⁻¹)
8498.02	-0.67 ± 0.03	-4.1 ± 0.4	19.8 ± 1.1
8542.09	-1.22 ± 0.03	-3.0 ± 0.3	21.1 ± 0.7
8662.14	-0.96 ± 0.03	-5.1 ± 0.4	22.9 ± 0.7

region of the atmosphere is undergoing atmospheric escape, but it does not rule it out for regions probed by other species that will be investigated in future analyses.

Whilst this is the first detection of the infrared Ca II triplet in the transmission spectrum of HAT-P-70 b, the near ultraviolet Ca II H and K lines were previously detected using HARPS-N at the TNG (Bello-Arufe et al. 2022), with line depths of $(-3.25 \pm 0.37)\%$ and $(-4.30 \pm 0.36)\%$ respectively. Such strong lines, seen for HAT-P-70 b as well as other UHJs, could be explained by hydrodynamic outflows causing a significant amount of Ca II to be transported into the upper atmosphere (Yan et al. 2019). We do not analyze the Ca II H and K lines in this initial study with GHOST due to the spectrograph focusing issue and the bluest wavelengths suffering from low SNR.

Since efforts were made to ensure that the spectra were combined in the planetary rest frame, any deviations of the measured Gaussian centroids from the rest-frame positions of the Ca II triplet lines should originate from physical processes within the atmosphere (although uncertainties in the ephemerides may also contribute, e.g. Stangret et al. 2024). The three Ca II lines are observed to be blueshifted by different amounts, between ~ 3 to 5 km s^{-1} along the line of sight, with non-overlapping error ranges. This suggests that strong dayside-to-nightside winds exist at multiple altitudes in the atmosphere of HAT-P-70 b, with a possible vertical change in velocity. These dynamical processes are typical of highly irradiated gas giants (e.g. Seidel et al. 2020, 2021, 2023a,b; Langeveld et al. 2022; Mounzer et al. 2022; Allart et al. 2023). Our measured velocities are also comparable to the other individually resolved spectral lines presented by Bello-Arufe et al. (2022).

Finally, we verified that the measured velocities are intrinsic to the planet and are not an artefact from instrumental drift. For all observed spectra, we isolated a region containing a number of strong telluric lines close to the Ca II triplet, between 8200–8300 Å, and performed a continuum normalization. We then followed the standard high-resolution cross-correlation method-

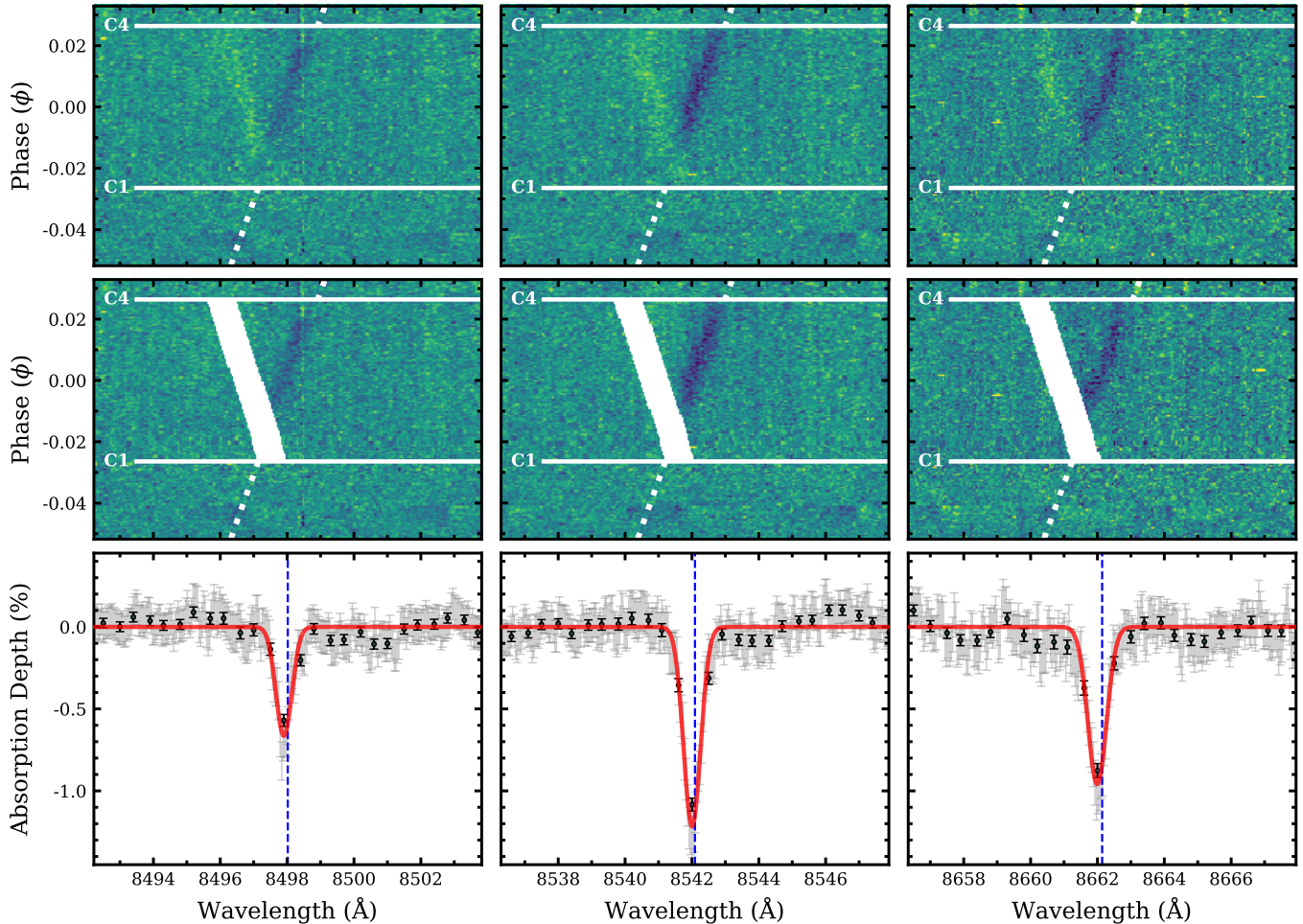


Figure 2. *Top row:* Residual spectra around the Ca II triplet lines after removing the telluric and stellar components, and dividing each observed spectrum by the master out-of-transit spectrum. The first (C1) and fourth (C4) transit contact points are marked with horizontal white lines, and the expected trails of the planetary atmospheric signals are highlighted by the white dotted lines (which are diagonal due to the Doppler motion of the planet). Atmospheric absorption from Ca II is clearly visible from the dark diagonal features following the projections of the expected planetary trails. The spurious features caused by the RM effect are visible as bright diagonal trails in the opposite direction. *Middle row:* Same as the top row, with the dominant RM trail masked out. The residual spectra now only contain the planetary signals. *Bottom row:* Combined transmission spectrum calculated using the weighted average of the in-transit data in the middle panel after Doppler shifting into the planetary rest frame. The data are displayed in their full resolution (grey) and binned 10 \times (black). Gaussian fits to the Ca II absorption lines are shown in red, and the blue dashed lines mark the expected position of the absorption lines in the planetary rest frame.

ology (e.g. Snellen et al. 2010; Birkby 2018), assigning the first spectrum as the “template” to cross-correlate with all other spectra, each time Doppler shifting the template between $\pm 50 \text{ km s}^{-1}$ in steps of 0.05 km s^{-1} . Gaussian profiles were then fitted to each exposure’s cross-correlation function, and the velocities corresponding to the maximum values of the fits were recorded – see Figure B1. This revealed a drift of $\sim 0.22 \text{ km s}^{-1}$ over the $\sim 5.5 \text{ hr}$ sequence of exposures, therefore negligible compared to the observed velocities discussed above, adding validity to the planetary origin.

4.2. Comparison with Non-Local Thermodynamic Equilibrium Atmospheric Models

The atmospheres of UHJs are expected to experience non-local thermodynamic equilibrium (NLTE) effects (e.g. Fossati et al. 2021), which can significantly impact the formation of spectral lines, particularly at the high altitudes (low pressures) probed by high-resolution spectroscopy (e.g. Young et al. 2024; Stangret et al. 2024). Moreover, the measured mass of HAT-P-70 b is only an upper limit (Zhou et al. 2019), so it is possible for the planet to have a lower mass, which in turn would lower

the bulk density and decrease the atmospheric pressure for the same altitude. We compared the detected Ca II triplet lines to NLTE models built using the framework of Young et al. (2024), updated to use the newly released Cloudy version 23.01 (Chatzikos et al. 2023). Using this framework, we created six NLTE atmospheric models: three with constant Ca abundance ($1\times$ solar) but varying planetary mass (the $6.78 M_J$ upper limit, $2 M_J$, and $1 M_J$); and three with constant planetary mass ($2 M_J$) but varying Ca abundance ($1\times$, $10\times$, and $100\times$ solar).

Figure 3 shows a comparison of these NLTE models to the observed Ca II triplet lines in the combined transmission spectrum, with the “constant abundance” models in the top panels and the “constant mass” on the bottom. To include the observed dayside-to-nightside atmospheric flow within the models, they were each shifted by the measured velocity offset of the Gaussian centroid for each line (listed in Table 1), and the x -axes are now displayed in velocity space.

For the constant abundance models, it is clear that $6.78 M_J$ is not a realistic mass for HAT-P-70 b, since the observed absorption lines are significantly deeper than simulated. The $2 M_J$ model slightly underestimates and the $1 M_J$ model slightly overestimates the observed line depths. Therefore, it is likely that the true mass of HAT-P-70 b lies somewhere in between these values – comparable to the mass of other UHJs that also show strong absorption features (e.g. WASP-76 b, WASP-121 b, WASP-189 b). This would also decrease the Roche lobe radius and bring the atmosphere closer to the evaporation regime. Further support for a lower mass planet is added by the fact that detecting spectral lines in the transmission spectra of high-gravity exoplanets has proven to be difficult and often unsuccessful (e.g. Wyttenbach et al. 2017; Stangret et al. 2021; Langeveld et al. 2022). A higher atmospheric temperature could also produce stronger absorption lines; however, the pressure-temperature profiles generated with these models already factor in a temperature that extends several thousands of degrees hotter at lower pressures than the equilibrium temperature.

These inferences are supported by high-resolution atmospheric retrievals that were performed on the transit observations of HAT-P-70 b with HARPS-N; with $\log(g)$ as a free parameter in the retrievals, Gandhi et al. (2023) constrained the planetary mass to $1.66 \pm 0.20 M_J$ (agreeing with our constraint from the NLTE models), albeit with the caveat that degeneracies in the retrieved parameters exist since the scale height of the atmosphere can also be affected by the temperature, the mean molecular weight of the atmosphere (which is assumed), and recombination of H to H_2 .

For the constant mass models, we fixed the mass to $2 M_J$ to investigate if a super-solar abundance could deepen the absorption and provide a closer match to the observations. However, as seen in the bottom panels of Figure 3, the wings of the absorption lines for the $10\times$ and $100\times$ solar models are much broader than perceived in the observations, with the $1\times$ solar abundance model more closely matching the line profiles in the data. Therefore, it is likely that the abundance of Ca in the atmosphere of HAT-P-70 b is approximately solar or subsolar. Incorporation of high-resolution atmospheric retrievals (e.g. Gandhi et al. 2023; Pelletier et al. 2023) with these GHOST data will provide clarity on this matter and will be explored in future work. Such retrieval frameworks extract the net atmospheric abundances utilizing the cross-correlation technique, and an atmospheric model of Ca II may include additional weaker absorbing lines over GHOST’s spectral range. Since the atmospheric pressure probed by absorption lines varies depending on the line depth (e.g. Young et al. 2024; Kesseli et al. 2024), retrievals may probe higher-pressure (deeper) regions of the atmosphere, where the abundance of Ca II may be different than the lower-pressure region probed by the triplet lines (as is expected based on the abundance profiles for multiple species in UHJ atmospheres, e.g. Fossati et al. 2021). Therefore, comparison of retrievals over different wavelength ranges provided by GHOST, or by selecting only the absorption lines within a certain range of depths, may provide further insight into the atmospheric structure and abundance of Ca II at different altitudes.

4.3. Time-Resolved Transmission Spectroscopy of the Individual Ca II Triplet Lines

The temporal variation of the atmospheric signals can be assessed by dividing the in-transit residual spectra (middle panel of Figure 2) into multiple bins, then combining the spectra within each phase bin to measure parameters of the Ca II lines from subsequent Gaussian fits (as performed in Section 4.1). To achieve this, phases from the transit ingress until $\phi \sim -0.01$ (where the RM and atmospheric signals overlap) were ignored, and the remaining data were divided equally into six groups of 10 spectra. The choice of six phase bins ensured that there are enough points to assess the temporal variation (with at least two bins before the mid-transit), and sufficient SNR within each bin to robustly resolve the Ca II lines and measure their parameters with Gaussian fits.

Figure 4 shows the variation of the measured absorption depths and velocity offsets of the three Ca II lines (orange, dark blue, and green points) across the six phase bins. The points circled in red highlight the phase

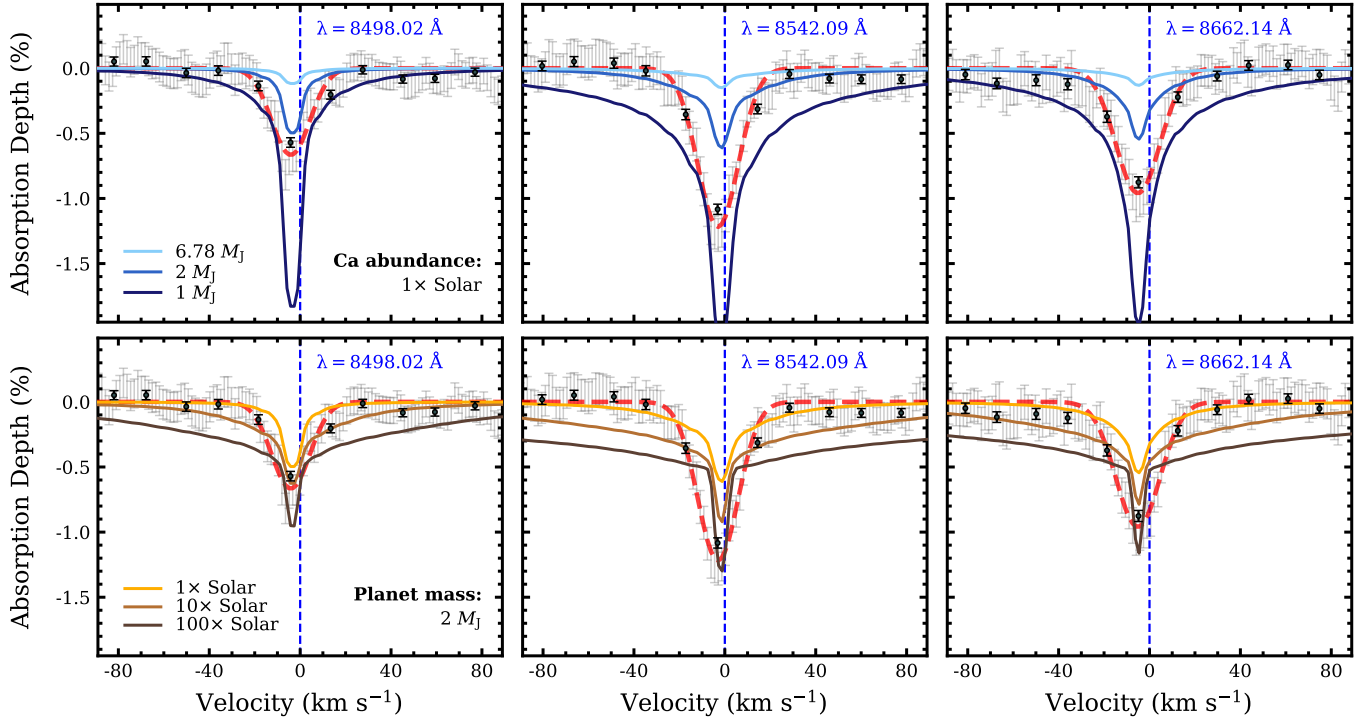


Figure 3. The Ca II triplet lines in the GHOST transmission spectrum of HAT-P-70 b compared to NLTE models generated for different planetary masses and Ca abundances. The same data from Figure 2 is displayed (full-resolution in grey, binned 10 \times in black, Gaussian fit in red), now in velocity space with the rest-frame line positions at 0 km s $^{-1}$. *Top row:* NLTE models for constant abundance (1 \times solar) and three different planetary masses (6.78 M_J , 2 M_J , and 1 M_J); the cores of the absorption lines become wider and deeper for decreasing masses. *Bottom row:* NLTE models for constant mass (2 M_J) and three different Ca abundances (1 \times , 10 \times and 100 \times solar); the line cores become deeper and the wings become wider for higher abundances.

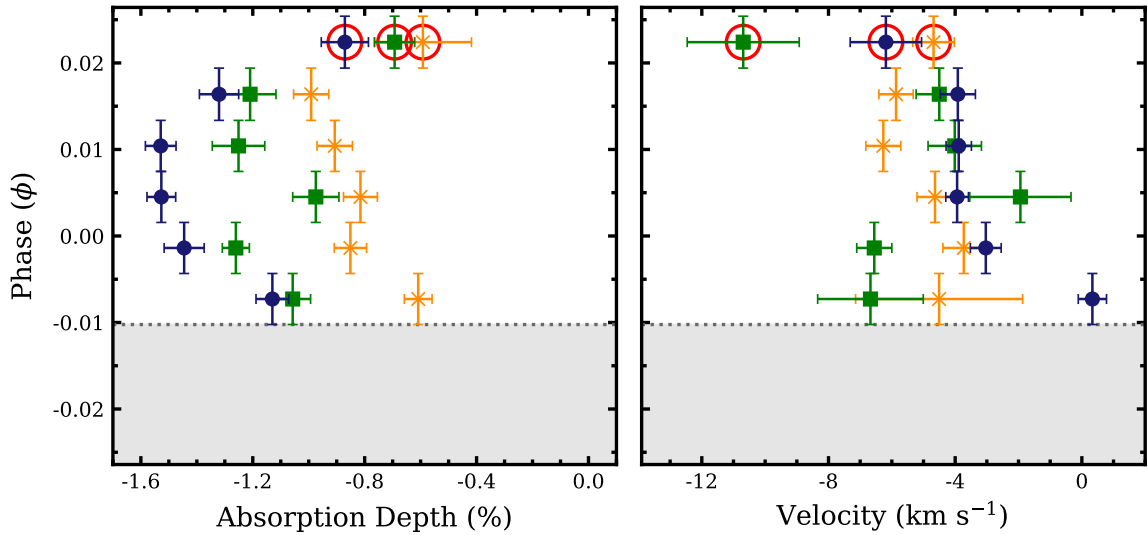


Figure 4. Variation of the measured absorption depths (*left*) and observed velocity offsets (*right*) of the three Ca II triplet lines at several phases throughout the transit of HAT-P-70 b. The phases where the RM features overlapped with the planetary absorption features were ignored (grey shaded region). The remaining in-transit residual spectra were binned into six groups, each containing 10 spectra that were subsequently combined with a weighted average. Each point is measured from Gaussian fits to the Ca II absorption lines with rest-frame positions at 8498.02 (orange crosses), 8542.09 (dark blue circles), and 8662.14 Å (green squares). Measurements for the egress phases (outlined with red circles) that probe mostly the trailing limb (evening terminator) show a distinct difference from the other phases – i.e. stronger blueshifted velocities and weaker absorption depths.

bin containing data obtained during the egress phases when the planet is partially transiting, thus it is mostly the trailing (evening) limb that contributes to these measurements. The phase bin closest to the masked-out region may not fully contain the atmospheric signal due to the proximity of nearby masked pixels, but we include them for completeness.

In general, the absorption depths of the Ca II lines stay between a range of around -1.6% (for the strongest line) to -0.9% (for the weakest line) across the transit, except for the egress phase bin where all three absorption lines become weaker. This is expected given that the transmission through the leading limb starts to disappear during the egress. Next, the observed line-of-sight velocities are distributed around a value of $\sim -4 \text{ km s}^{-1}$ throughout the transit, except again for the egress phase bin where they are more blueshifted on average. The extra blueshift may be attributed to: (1) stronger dayside-to-nightside winds at the evening terminator driven by an eastwards advection of the hottest region of the atmosphere from the substellar point (the strength of which may depend on atmospheric processes such as hydrogen dissociation/recombination, internal heat flux, or magnetic drag, e.g. Tan & Komacek 2019; Komacek et al. 2022; Beltz et al. 2022, 2023; Beltz & Rauscher 2024); and/or (2) the Doppler shift of the atmospheric signals from only the blueshifted side of the planet due to the tidally locked planetary rotation (Wardenier et al. 2021, 2022). The rotational velocity of the atmosphere assuming tidally locked rotation ranges from zero (at the poles) to a maximum (at the equator) of $\sim 3.5 \text{ km s}^{-1}$ for the bulk planetary radius, or $\sim 5.1 \text{ km s}^{-1}$ for the extended atmospheric radius probed by the deepest Ca II line – these values roughly match the average velocity difference at egress seen in Figure 4 (compared to the rest of the transit), however, we cannot rule out stronger evening terminator winds without more robust measurements across multiple species. Similar detections have been made for other highly irradiated gas giant exoplanets (e.g. Louden & Wheatley 2015; Ehrenreich et al. 2020). Therefore, not only can these GHOST data constrain net dayside-to-nightside atmospheric wind speeds from the Ca II lines in the combined transmission spectrum, but the time-resolved measurements now provide independent spatial information about the different limbs.

Time-resolved high-resolution transmission spectroscopy of the UHJ WASP-76 b previously revealed an asymmetric shape to the cross-correlated Fe I absorption trail throughout the transit, where the signal gradually became more blueshifted until around the mid-transit, after which it remained at a constant velocity (Ehrenreich et al. 2020).

This was explained by Fe I being localized to a region closer to the evening terminator than the morning, and the rotation of the planet aligning this region such that absorption occurs only within the evening terminator during the entire second half of the transit (thus at a constant velocity). These asymmetries were also confirmed to be present at different altitudes within the atmosphere of WASP-76 b from an analysis of the cross-correlated signal for weak (low altitude), medium, and strong (high altitude) Fe I lines separately (Kesseli et al. 2024) – tentative signs of stronger blueshifts at lower altitudes were also reported, in agreement with inferences made from the analysis of the Na doublet (Seidel et al. 2021). In contrast, these time-resolved detections of the individual Ca II lines for HAT-P-70 b show that the velocity values are overall more blueshifted only at the egress phases, suggesting that Ca II is at least partially visible through the leading limb at all phases except when it starts to egress, thus it is distributed across the entire terminator. The signals nearest the masked-out region may suggest some asymmetry in the strength of the lines as well as their Doppler shift; however, we cannot make a significant conclusion about this without a robust removal of the RM signals near ingress.

5. CONCLUSION

This work demonstrates the capabilities of the new Gemini High-resolution Optical SpecTrograph (GHOST) at the Gemini South Observatory for investigating the 3D nature of exoplanet atmospheres. In this first transmission spectroscopy study with the high-resolution mode GHOST, we observed one transit of the ultra-hot Jupiter HAT-P-70 b and made new detections of the infrared Ca II triplet absorption lines, complementing previous detections of the near ultraviolet Ca II H and K lines (Bello-Arufe et al. 2022). From Gaussian fits to the three absorption lines, we inferred: (1) that Ca II in the planetary atmosphere extends to the upper altitudes of the planetary atmosphere at a height of at least 0.47 times the bulk planetary radius R_p ; and (2) that the three lines are blueshifted, varying between ~ 3 to 5 km s^{-1} along the line of sight, which is indicative of strong dayside-to-nightside winds with a possible velocity gradient between different altitudes. Comparing the combined transmission spectrum with NLTE atmospheric models generated for HAT-P-70 b revealed that the planetary mass is likely to be around $1\text{--}2 M_J$ (much lighter than the $6.78 M_J$ upper limit measured from radial velocities), and that the abundance of Ca within the atmosphere is solar or subsolar.

Most notably, capitalizing on the high SNR achieved by GHOST and Gemini South, we showed that the indi-

vidual Ca II absorption lines can be temporally resolved to analyze how the absorption through the terminator changes throughout the transit, allowing different planetary longitudes to be probed (due to rotation of the tidally locked planet). During the transit egress, where the signals mostly originate from the trailing limb (evening terminator), the absorption strength decreased (due to the loss of signal from the leading limb) and the velocities became more blueshifted on average (due to the planet rotating towards the observer at the trailing limb and stronger winds driven by the hotspot being offset eastwards from the substellar point). Besides the egress phases, we saw no clear evidence of asymmetries in the velocity measurements, suggesting that Ca II is distributed at least partially on both the morning and evening terminators. However, this needs to be confirmed with a robust correction of the spurious signals produced by the Rossiter-McLaughlin effect that obscure the atmospheric signals near the planetary ingress.

Time-resolved detections are paramount for advancing our understanding of the complex chemical and dynamical processes in UHJ atmospheres, and they provide crucial contributions towards inferences made with high-resolution atmospheric retrievals and general circulation models. However, the high SNR required for time-resolved detections of individual spectral lines (i.e. without relying on the cross-correlation technique) is only feasible with the latest state-of-the-art high-resolution spectrographs at 8–10 m class telescopes. Therefore, this demonstration places GHOST among the few instruments that can achieve these goals.

ACKNOWLEDGMENTS

We thank the anonymous referee for their constructive and thoughtful comments, which helped to improve this manuscript.

The authors thank the observers at Gemini South for the data acquisition (Venu Kalari, Lindsay Magill, Daniel May, and Henrique Reggiani), and Jeong-Eun Heo (program contact scientist with EKD).

Based on observations obtained under Program ID GS-2023B-FT-105 at the international Gemini Observa-

tory, a program of NSF NOIRLab, which is managed by the Association of Universities for Research in Astronomy (AURA) under a cooperative agreement with the U.S. National Science Foundation on behalf of the Gemini Observatory partnership: the U.S. National Science Foundation (United States), National Research Council (Canada), Agencia Nacional de Investigación y Desarrollo (Chile), Ministerio de Ciencia, Tecnología e Innovación (Argentina), Ministério da Ciência, Tecnologia, Inovações e Comunicações (Brazil), and Korea Astronomy and Space Science Institute (Republic of Korea). Data processed using DRAGONS (Data Reduction for Astronomy from Gemini Observatory North and South).

GHOST was built by a collaboration between Australian Astronomical Optics at Macquarie University, National Research Council Herzberg of Canada, and the Australian National University. The instrument scientist is Dr. Alan McConnachie at NRC, and the instrument team is also led by Dr. Gordon Robertson (at AAO), and Dr. Michael Ireland (at ANU).

EKD acknowledges the support of the Natural Sciences and Engineering Research Council of Canada (NSERC), funding reference No. 568281-2022.

EdM and MY acknowledge support from the Science and Technology Facilities Council (STFC) award ST/X00094X/1.

JDT acknowledges funding support by the TESS Guest Investigator Program G06165.

Facilities: Gemini:South (GHOST)

Software: GHOSTDR (Ireland et al. 2018; Hayes et al. 2022), DRAGONS (Labrie et al. 2023), molecfit (Smette et al. 2015; Kausch et al. 2015), Cloudy (Chatzikos et al. 2023), Astropy (Astropy Collaboration et al. 2013, 2018, 2022), NumPy (Harris et al. 2020), SciPy (Virtanen et al. 2020), Matplotlib (Hunter 2007)

APPENDIX

A. SYSTEM PARAMETERS

The parameters adopted during the extraction and analysis of the HAT-P-70 b transmission spectrum are listed in Table A1. There is only an upper limit for the planetary mass (and therefore planetary RV semi-amplitude).

B. INSTRUMENTAL DRIFT

The instrumental drift of GHOST over the ~ 5.5 hr sequence of exposures was measured as described in Section 4.1 and illustrated in Figure B1. The measured drift is negligible compared to observed velocity offsets of the spectral lines from the atmosphere of HAT-P-70 b.

Table A1. Stellar, planetary, and orbital parameters adopted in this work for the HAT-P-70 system. Derived parameters: (†) Calculated using $K_p = -K_*(M_*/M_p)$, but due to the constraints on K_* and M_p , this value is derived using the upper limit of both parameters; (‡) Calculated using $T_{\text{eq}} = T_{\text{eff}} [(1 - f_r)(1 - A_B)R_*^2/(2a^2)]^{1/4}$, assuming uniform heat redistribution ($f_r = 0.5$), zero bond albedo, and a circular orbit.

Parameter	Symbol	Value	Unit	Reference
Star				
Stellar Mass	M_*	$1.890^{+0.010}_{-0.013}$	M_\odot	Zhou et al. (2019)
Stellar Radius	R_*	$1.858^{+0.119}_{-0.091}$	R_\odot	Zhou et al. (2019)
Stellar RV Semi-amplitude	K_*	< 649	m s^{-1}	Zhou et al. (2019)
Effective Temperature	T_{eff}	8450^{+540}_{-690}	K	Zhou et al. (2019)
Projected Rotational Velocity	$v \sin i$	$99.85^{+0.64}_{-0.61}$	km s^{-1}	Zhou et al. (2019)
Surface Gravity	$\log g$	$4.181^{+0.055}_{-0.063}$	$\log_{10}(\text{cm s}^{-2})$	Zhou et al. (2019)
Metallicity	[Fe/H]	$-0.059^{+0.075}_{-0.088}$	dex	Zhou et al. (2019)
Planet				
Planetary Mass	M_p	< 6.78	M_J	Zhou et al. (2019)
Planetary Radius	R_p	$1.87^{+0.15}_{-0.10}$	R_J	Zhou et al. (2019)
Planetary RV Semi-amplitude	K_p	-190	km s^{-1}	Derived †
Equilibrium Temperature	T_{eq}	2550^{+180}_{-220}	K	Derived ‡
Orbital Inclination	i_p	$96.50^{+1.42}_{-0.91}$	deg	Zhou et al. (2019)
Sky Projected Obliquity	λ	$113.1^{+5.1}_{-3.4}$	deg	Zhou et al. (2019)
System				
Period	P	$2.744320^{+0.000001}_{-0.000001}$	days	Ivshina & Winn (2022)
Mid-transit Time	T_c	$2459175.05277^{+0.00017}_{-0.00017}$	BJD	Ivshina & Winn (2022)
Transit Duration	T_{14}	$0.145^{+0.003}_{-0.002}$	days	Zhou et al. (2019)
Semi-major Axis	a	$0.04739^{+0.00031}_{-0.00106}$	au	Zhou et al. (2019)
Systemic Velocity	v_{sys}	$25.260^{+0.110}_{-0.110}$	km s^{-1}	Zhou et al. (2019)

REFERENCES

- Allart, R., Lovis, C., Pino, L., et al. 2017, *A&A*, 606, A144, doi: [10.1051/0004-6361/201730814](https://doi.org/10.1051/0004-6361/201730814)
- Allart, R., Lemée-Joliecoeur, P. B., Jaziri, A. Y., et al. 2023, *A&A*, 677, A164, doi: [10.1051/0004-6361/202245832](https://doi.org/10.1051/0004-6361/202245832)
- Arcangeli, J., Désert, J.-M., Line, M. R., et al. 2018, *ApJL*, 855, L30, doi: [10.3847/2041-8213/aab272](https://doi.org/10.3847/2041-8213/aab272)
- Astropy Collaboration, Robitaille, T. P., Tollerud, E. J., et al. 2013, *A&A*, 558, A33, doi: [10.1051/0004-6361/201322068](https://doi.org/10.1051/0004-6361/201322068)
- Astropy Collaboration, Price-Whelan, A. M., Sipőcz, B. M., et al. 2018, *AJ*, 156, 123, doi: [10.3847/1538-3881/aabc4f](https://doi.org/10.3847/1538-3881/aabc4f)
- Astropy Collaboration, Price-Whelan, A. M., Lim, P. L., et al. 2022, *ApJ*, 935, 167, doi: [10.3847/1538-4357/ac7c74](https://doi.org/10.3847/1538-4357/ac7c74)
- Bell, T. J., & Cowan, N. B. 2018, *ApJL*, 857, L20, doi: [10.3847/2041-8213/aabcc8](https://doi.org/10.3847/2041-8213/aabcc8)
- Bello-Arufe, A., Cabot, S. H. C., Mendonça, J. M., Buchhave, L. A., & Rathcke, A. D. 2022, *AJ*, 163, 96, doi: [10.3847/1538-3881/ac402e](https://doi.org/10.3847/1538-3881/ac402e)
- Beltz, H., & Rauscher, E. 2024, *ApJ*, 976, 32, doi: [10.3847/1538-4357/ad7ded](https://doi.org/10.3847/1538-4357/ad7ded)
- Beltz, H., Rauscher, E., Kempton, E. M. R., Malsky, I., & Savel, A. B. 2023, *AJ*, 165, 257, doi: [10.3847/1538-3881/acd24d](https://doi.org/10.3847/1538-3881/acd24d)
- Beltz, H., Rauscher, E., Roman, M. T., & Guilliat, A. 2022, *AJ*, 163, 35, doi: [10.3847/1538-3881/ac3746](https://doi.org/10.3847/1538-3881/ac3746)
- Birkby, J. L. 2018, arXiv e-prints, arXiv:1806.04617, doi: [10.48550/arXiv.1806.04617](https://doi.org/10.48550/arXiv.1806.04617)

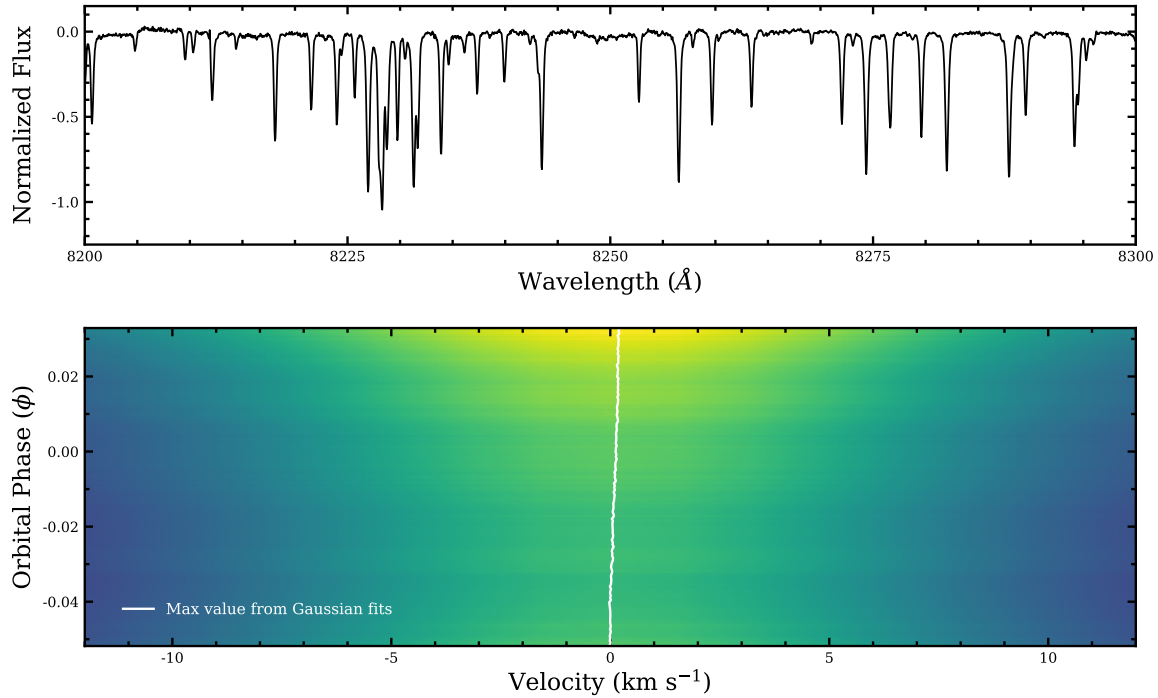


Figure B1. The instrumental drift of GHOST for the duration of these observations. *Top panel:* isolated region of the spectrum (continuum normalized) containing a number of strong telluric lines that was used as a template for the cross-correlation analysis. *Bottom panel:* result after cross-correlating each observed spectrum with the template (Doppler shifted between $\pm 50 \text{ km s}^{-1}$ in steps of 0.05 km s^{-1}), displayed in phase–velocity space. Brighter colours indicate a stronger correlation. The maximum value of each cross-correlation function (each row), measured with Gaussian fits, is marked by the white line; the total drift is $\sim 0.22 \text{ km s}^{-1}$ over the sequence of exposures.

- Boldt-Christmas, L., Lesjak, F., Wehrhahn, A., et al. 2024, *A&A*, 683, A244, doi: [10.1051/0004-6361/202347398](https://doi.org/10.1051/0004-6361/202347398)
- Borsa, F., Allart, R., Casasayas-Barris, N., et al. 2021, *A&A*, 645, A24, doi: [10.1051/0004-6361/202039344](https://doi.org/10.1051/0004-6361/202039344)
- Borsato, N. W., Hoeijmakers, H. J., Prinoth, B., et al. 2023, *A&A*, 673, A158, doi: [10.1051/0004-6361/202245121](https://doi.org/10.1051/0004-6361/202245121)
- Casasayas-Barris, N., Pallé, E., Yan, F., et al. 2020, *A&A*, 635, A206, doi: [10.1051/0004-6361/201937221](https://doi.org/10.1051/0004-6361/201937221)
- Casasayas-Barris, N., Pallé, E., Stangret, M., et al. 2021, *A&A*, 647, A26, doi: [10.1051/0004-6361/202039539](https://doi.org/10.1051/0004-6361/202039539)
- Chatzikos, M., Bianchi, S., Camilloni, F., et al. 2023, *RMxAA*, 59, 327, doi: [10.22201/ia.01851101p.2023.59.02.12](https://doi.org/10.22201/ia.01851101p.2023.59.02.12)
- Deibert, E. K., de Mooij, E. J. W., Jayawardhana, R., et al. 2021, *ApJL*, 919, L15, doi: [10.3847/2041-8213/ac2513](https://doi.org/10.3847/2041-8213/ac2513)
- Deibert, E. K., Langeveld, A. B., Young, M. E., et al. 2024, *AJ*, 168, 148, doi: [10.3847/1538-3881/ad643f](https://doi.org/10.3847/1538-3881/ad643f)
- Dethier, W., & Bourrier, V. 2023, *A&A*, 674, A86, doi: [10.1051/0004-6361/202245705](https://doi.org/10.1051/0004-6361/202245705)
- Eggleton, P. P. 1983, *ApJ*, 268, 368, doi: [10.1086/160960](https://doi.org/10.1086/160960)
- Ehrenreich, D., Lovis, C., Allart, R., et al. 2020, *Nature*, 580, 597, doi: [10.1038/s41586-020-2107-1](https://doi.org/10.1038/s41586-020-2107-1)
- Fossati, L., Young, M. E., Shulyak, D., et al. 2021, *A&A*, 653, A52, doi: [10.1051/0004-6361/202140813](https://doi.org/10.1051/0004-6361/202140813)
- Gandhi, S., Kesseli, A., Snellen, I., et al. 2022, *MNRAS*, 515, 749, doi: [10.1093/mnras/stac1744](https://doi.org/10.1093/mnras/stac1744)
- Gandhi, S., Kesseli, A., Zhang, Y., et al. 2023, *AJ*, 165, 242, doi: [10.3847/1538-3881/accd65](https://doi.org/10.3847/1538-3881/accd65)
- Gaudi, B. S., & Winn, J. N. 2007, *ApJ*, 655, 550, doi: [10.1086/509910](https://doi.org/10.1086/509910)
- Harris, C. R., Millman, K. J., van der Walt, S. J., et al. 2020, *Nature*, 585, 357, doi: [10.1038/s41586-020-2649-2](https://doi.org/10.1038/s41586-020-2649-2)
- Hayes, C. R., Waller, F., Ireland, M., et al. 2022, in *Society of Photo-Optical Instrumentation Engineers (SPIE) Conference Series*, Vol. 12184, *Ground-based and Airborne Instrumentation for Astronomy IX*, ed. C. J. Evans, J. J. Bryant, & K. Motohara, 121846H, doi: [10.1117/12.2642905](https://doi.org/10.1117/12.2642905)
- Heng, K., & Showman, A. P. 2015, *Annual Review of Earth and Planetary Sciences*, 43, 509, doi: [10.1146/annurev-earth-060614-105146](https://doi.org/10.1146/annurev-earth-060614-105146)
- Hunter, J. D. 2007, *Computing in Science & Engineering*, 9, 90, doi: [10.1109/MCSE.2007.55](https://doi.org/10.1109/MCSE.2007.55)

- Ireland, M., Anthony, A., Burley, G., et al. 2014, in *Society of Photo-Optical Instrumentation Engineers (SPIE) Conference Series*, Vol. 9147, *Ground-based and Airborne Instrumentation for Astronomy V*, ed. S. K. Ramsay, I. S. McLean, & H. Takami, 91471J, doi: [10.1117/12.2057356](https://doi.org/10.1117/12.2057356)
- Ireland, M. J., White, M., Bento, J. P., et al. 2018, in *Society of Photo-Optical Instrumentation Engineers (SPIE) Conference Series*, Vol. 10707, *Software and Cyberinfrastructure for Astronomy V*, ed. J. C. Guzman & J. Ibsen, 1070735, doi: [10.1117/12.2314418](https://doi.org/10.1117/12.2314418)
- Ireland, M. J., Barnes, S., Cochrane, D., et al. 2012, in *Society of Photo-Optical Instrumentation Engineers (SPIE) Conference Series*, Vol. 8446, *Ground-based and Airborne Instrumentation for Astronomy IV*, ed. I. S. McLean, S. K. Ramsay, & H. Takami, 844629, doi: [10.1117/12.925746](https://doi.org/10.1117/12.925746)
- Ivshina, E. S., & Winn, J. N. 2022, *ApJS*, 259, 62, doi: [10.3847/1538-4365/ac545b](https://doi.org/10.3847/1538-4365/ac545b)
- Kalari, V. M., Diaz, R. J., Robertson, G., et al. 2024, *AJ*, 168, 208, doi: [10.3847/1538-3881/ad72ed](https://doi.org/10.3847/1538-3881/ad72ed)
- Kausch, W., Noll, S., Smette, A., et al. 2015, *A&A*, 576, A78, doi: [10.1051/0004-6361/201423909](https://doi.org/10.1051/0004-6361/201423909)
- Kesseli, A. Y., Beltz, H., Rauscher, E., & Snellen, I. A. G. 2024, *ApJ*, 975, 9, doi: [10.3847/1538-4357/ad772f](https://doi.org/10.3847/1538-4357/ad772f)
- Kesseli, A. Y., & Snellen, I. A. G. 2021, *ApJL*, 908, L17, doi: [10.3847/2041-8213/abe047](https://doi.org/10.3847/2041-8213/abe047)
- Kesseli, A. Y., Snellen, I. A. G., Casasayas-Barris, N., Mollière, P., & Sánchez-López, A. 2022, *AJ*, 163, 107, doi: [10.3847/1538-3881/ac4336](https://doi.org/10.3847/1538-3881/ac4336)
- Kitzmann, D., Heng, K., Rimmer, P. B., et al. 2018, *ApJ*, 863, 183, doi: [10.3847/1538-4357/aace5a](https://doi.org/10.3847/1538-4357/aace5a)
- Komacek, T. D., Gao, P., Thorngren, D. P., May, E. M., & Tan, X. 2022, *ApJL*, 941, L40, doi: [10.3847/2041-8213/aca975](https://doi.org/10.3847/2041-8213/aca975)
- Labrie, K., Simpson, C., Cardenas, R., et al. 2023, *Research Notes of the American Astronomical Society*, 7, 214, doi: [10.3847/2515-5172/ad0044](https://doi.org/10.3847/2515-5172/ad0044)
- Langeveld, A. B., Madhusudhan, N., & Cabot, S. H. C. 2022, *MNRAS*, 514, 5192, doi: [10.1093/mnras/stac1539](https://doi.org/10.1093/mnras/stac1539)
- Langeveld, A. B., Madhusudhan, N., Cabot, S. H. C., & Hodgkin, S. T. 2021, *MNRAS*, 502, 4392, doi: [10.1093/mnras/stab134](https://doi.org/10.1093/mnras/stab134)
- Louden, T., & Wheatley, P. J. 2015, *ApJL*, 814, L24, doi: [10.1088/2041-8205/814/2/L24](https://doi.org/10.1088/2041-8205/814/2/L24)
- McConnachie, A. W., Hayes, C. R., Robertson, J. G., et al. 2024, *PASP*, 136, 035001, doi: [10.1088/1538-3873/ad1ed4](https://doi.org/10.1088/1538-3873/ad1ed4)
- McLaughlin, D. B. 1924, *ApJ*, 60, 22, doi: [10.1086/142826](https://doi.org/10.1086/142826)
- Mounzer, D., Lovis, C., Seidel, J. V., et al. 2022, *A&A*, 668, A1, doi: [10.1051/0004-6361/202243998](https://doi.org/10.1051/0004-6361/202243998)
- Nortmann, L., Lesjak, F., Yan, F., et al. 2025, *A&A*, 693, A213, doi: [10.1051/0004-6361/202450438](https://doi.org/10.1051/0004-6361/202450438)
- Parmentier, V., Line, M. R., Bean, J. L., et al. 2018, *A&A*, 617, A110, doi: [10.1051/0004-6361/201833059](https://doi.org/10.1051/0004-6361/201833059)
- Pelletier, S., Benneke, B., Ali-Dib, M., et al. 2023, *Nature*, 619, 491, doi: [10.1038/s41586-023-06134-0](https://doi.org/10.1038/s41586-023-06134-0)
- Prinoth, B., Hoeijmakers, H. J., Pelletier, S., et al. 2023, *A&A*, 678, A182, doi: [10.1051/0004-6361/202347262](https://doi.org/10.1051/0004-6361/202347262)
- Prinoth, B., Hoeijmakers, H. J., Morris, B. M., et al. 2024, *A&A*, 685, A60, doi: [10.1051/0004-6361/202349125](https://doi.org/10.1051/0004-6361/202349125)
- Rauscher, E., & Kempton, E. M. R. 2014, *ApJ*, 790, 79, doi: [10.1088/0004-637X/790/1/79](https://doi.org/10.1088/0004-637X/790/1/79)
- Rossiter, R. A. 1924, *ApJ*, 60, 15, doi: [10.1086/142825](https://doi.org/10.1086/142825)
- Savel, A. B., Kempton, E. M. R., Rauscher, E., et al. 2023, *ApJ*, 944, 99, doi: [10.3847/1538-4357/acb141](https://doi.org/10.3847/1538-4357/acb141)
- Savel, A. B., Kempton, E. M. R., Malik, M., et al. 2022, *ApJ*, 926, 85, doi: [10.3847/1538-4357/ac423f](https://doi.org/10.3847/1538-4357/ac423f)
- Seidel, J. V., Ehrenreich, D., Pino, L., et al. 2020, *A&A*, 633, A86, doi: [10.1051/0004-6361/201936892](https://doi.org/10.1051/0004-6361/201936892)
- Seidel, J. V., Prinoth, B., Knudstrup, E., et al. 2023a, *A&A*, 678, A150, doi: [10.1051/0004-6361/202347160](https://doi.org/10.1051/0004-6361/202347160)
- Seidel, J. V., Ehrenreich, D., Allart, R., et al. 2021, *A&A*, 653, A73, doi: [10.1051/0004-6361/202140569](https://doi.org/10.1051/0004-6361/202140569)
- Seidel, J. V., Borsa, F., Pino, L., et al. 2023b, *A&A*, 673, A125, doi: [10.1051/0004-6361/202245800](https://doi.org/10.1051/0004-6361/202245800)
- Showman, A. P., Cooper, C. S., Fortney, J. J., & Marley, M. S. 2008, *ApJ*, 682, 559, doi: [10.1086/589325](https://doi.org/10.1086/589325)
- Showman, A. P., Tan, X., & Parmentier, V. 2020, *SSRv*, 216, 139, doi: [10.1007/s11214-020-00758-8](https://doi.org/10.1007/s11214-020-00758-8)
- Simonnin, A., Parmentier, V., Wardenier, J. P., et al. 2024, *arXiv e-prints*, arXiv:2412.01472, doi: [10.48550/arXiv.2412.01472](https://doi.org/10.48550/arXiv.2412.01472)
- Smette, A., Sana, H., Noll, S., et al. 2015, *A&A*, 576, A77, doi: [10.1051/0004-6361/201423932](https://doi.org/10.1051/0004-6361/201423932)
- Snellen, I. A. G., de Kok, R. J., de Mooij, E. J. W., & Albrecht, S. 2010, *Nature*, 465, 1049, doi: [10.1038/nature09111](https://doi.org/10.1038/nature09111)
- Stangret, M., Pallé, E., Casasayas-Barris, N., et al. 2021, *A&A*, 654, A73, doi: [10.1051/0004-6361/202040100](https://doi.org/10.1051/0004-6361/202040100)
- Stangret, M., Fossati, L., D'Arpa, M. C., et al. 2024, *A&A*, 692, A76, doi: [10.1051/0004-6361/202451277](https://doi.org/10.1051/0004-6361/202451277)
- Tabernerero, H. M., Zapatero Osorio, M. R., Allart, R., et al. 2021, *A&A*, 646, A158, doi: [10.1051/0004-6361/202039511](https://doi.org/10.1051/0004-6361/202039511)
- Tan, X., & Komacek, T. D. 2019, *ApJ*, 886, 26, doi: [10.3847/1538-4357/ab4a76](https://doi.org/10.3847/1538-4357/ab4a76)
- Triaud, A. H. M. J. 2018, in *Handbook of Exoplanets*, ed. H. J. Deeg & J. A. Belmonte (Springer International Publishing AG), 2, doi: [10.1007/978-3-319-55333-7_2](https://doi.org/10.1007/978-3-319-55333-7_2)

- Turner, J. D., de Mooij, E. J. W., Jayawardhana, R., et al. 2020, *ApJL*, 888, L13, doi: [10.3847/2041-8213/ab60a9](https://doi.org/10.3847/2041-8213/ab60a9)
- Virtanen, P., Gommers, R., Oliphant, T. E., et al. 2020, *Nature Methods*, 17, 261, doi: [10.1038/s41592-019-0686-2](https://doi.org/10.1038/s41592-019-0686-2)
- Wardenier, J. P., Parmentier, V., & Lee, E. K. H. 2022, *MNRAS*, 510, 620, doi: [10.1093/mnras/stab3432](https://doi.org/10.1093/mnras/stab3432)
- Wardenier, J. P., Parmentier, V., Lee, E. K. H., Line, M. R., & Gharib-Nezhad, E. 2021, *MNRAS*, 506, 1258, doi: [10.1093/mnras/stab1797](https://doi.org/10.1093/mnras/stab1797)
- Wardenier, J. P., Parmentier, V., Line, M. R., et al. 2024, *PASP*, 136, 084403, doi: [10.1088/1538-3873/ad5c9f](https://doi.org/10.1088/1538-3873/ad5c9f)
- Wytttenbach, A., Ehrenreich, D., Lovis, C., Udry, S., & Pepe, F. 2015, *A&A*, 577, A62, doi: [10.1051/0004-6361/201525729](https://doi.org/10.1051/0004-6361/201525729)
- Wytttenbach, A., Lovis, C., Ehrenreich, D., et al. 2017, *A&A*, 602, A36, doi: [10.1051/0004-6361/201630063](https://doi.org/10.1051/0004-6361/201630063)
- Yan, F., Casasayas-Barris, N., Molaverdikhani, K., et al. 2019, *A&A*, 632, A69, doi: [10.1051/0004-6361/201936396](https://doi.org/10.1051/0004-6361/201936396)
- Young, M. E., Spring, E. F., & Birkby, J. L. 2024, *MNRAS*, 530, 4356, doi: [10.1093/mnras/stae674](https://doi.org/10.1093/mnras/stae674)
- Zhou, G., Huang, C. X., Bakos, G. Á., et al. 2019, *AJ*, 158, 141, doi: [10.3847/1538-3881/ab36b5](https://doi.org/10.3847/1538-3881/ab36b5)